Nanoscale

Mapping the phase-separated state in a 2D magnet

Journal:	*Nanoscale*
Manuscript ID	NR-ART-12-2023-006550.R1
Article Type:	Paper
Date Submitted by the Author:	13-Feb-2024

Complete List of Authors:	Mattiat, Hinrich; University of Basel Schneider, Lukas; University of Basel Reiser, Patrick; University of Basel, Poggio, Martino; University of Basel, Department of Physics Sahafi, Pardis; University of Waterloo, ; National Research Council Canada, Jordan, Andrew; University of Waterloo Budakian, Raffi; University of Waterloo Averyanov, Dmitry; Kurchatov Institute, Sokolov, Ivan; Kurchatov Institute, Taldenkov, Alexander; Kurchatov Institute Parfenov, Oleg; Kurchatov Institute, Kondratev, Oleg; National Research Center Kurchatov Institute, Tokmachev, Andrey; Kurchatov Institute, Storchak, Vyacheslav; Kurchatov Institute,

SCHOLARONE™
Manuscripts

Please do not adjust margins

PAPER

Mapping the phase-separated state in a 2D magnet

Received 00th January 20xx,
Accepted 00th January 20xx

DOI: 10.1039/x0xx00000x

Hinrich Mattiat,[1,§] Lukas Schneider,[1,§] Patrick Reiser,[1] Martino Poggio,[1,*] Pardis Sahafi,[2,#] Andrew Jordan,[2] Raffi Budakian,[2] Dmitry V. Averyanov,[3] Ivan S. Sokolov,[3] Alexander N. Taldenkov,[3] Oleg E. Parfenov,[3] Oleg A. Kondratev,[3] Andrey M. Tokmachev,[3] Vyacheslav G. Storchak[3,*]

Intrinsic 2D magnets have recently been established as a playground for studies on fundamentals of magnetism, quantum phases, and spintronic applications. The inherent instability at low dimensionality often results in coexistence and/or competition of different magnetic orders. Such instability of magnetic ordering may manifest itself as phase-separated states. In 4*f* 2D materials, magnetic phase separation is expressed in various experiments; however, the experimental evidence is circumstantial. Here, we employ a high-sensitivity MFM technique to probe the spatial distribution of magnetic states in the paradigmatic 4*f* 2D ferromagnet $EuGe_2$. Below the ferromagnetic transition temperature, we discover the phase-separated state and follow its evolution with temperature and magnetic field. The characteristic length-scale of magnetic domains amounts to hundreds of nanometers. These observations strongly shape our understanding of the magnetic states in 2D materials at the monolayer limit and contribute to engineering of ultra-compact spintronics.

Introduction

Advances in synthesis and fabrication of functional materials have pushed the research frontier in magnetism to the 2D limit.[1-3] The interest in 2D magnetism is both fundamental and practical. The former is associated with the emergence of exotic quantum phases and magnetic ground states whereas the latter suggests technological advances: being key elements in spintronic devices,[4] 2D magnets meet the demands for ultra-compact electronics. An important advantage of many 2D magnets is their employment in multifunctional van-der-Waals heterostructures.[1-3] The research field is rather young but is being actively developed. One of the reasons is the ubiquity of the phenomenon as many 2D materials exhibit magnetic properties: *d*-element,[5-7] *f*-element,[8,9] and more exotic *p*-element[10,11] compounds. Another reason is that the magnetic states in 2D magnets are highly amenable to external stimuli.[12] The states can be controlled by magnetic fields,[6] pressure[13] or gating.[14] In particular, strong response to magnetic fields affects the electron transport properties in 2D magnets, resulting in giant tunneling magnetoresistance[15] and colossal lateral magnetoresistance.[16]

Unlike most 3D magnetic materials, 2D magnets often demonstrate coexistence of magnetic orders promoted by reduced dimensionality. In 2D systems, instability of magnetic ordering and competition between magnetic phases may result in phase-separated states, similar to those in manganites with colossal magnetoresistance[17] or dilute magnetic semiconductors.[18] Also, phase-separated states are likely to be responsible for the observation of antagonistic ferromagnetism (FM) and superconductivity in the same layer.[19] Coexisting FM and antiferromagnetic (AFM) orders in a 2D magnet can be brought about by moiré engineering,[20,21] chemical modification[22,23] or external pressure;[24] in fact, more than 2 magnetic phases may coexist.[24] A key parameter affecting the magnetic order is the number of monolayers (ML): a number of compounds demonstrate transformation of 3D AFM in the bulk into 2D FM in a single ML. This behaviour, exhibited by $MnBi_2Te_4$,[25] $MnSb_2Te_4$,[26] $CrCl_3$,[27] CrSBr,[28] the oxides NiO[29] and Fe_2O_3,[7] is often associated with different intralayer (FM) and interlayer (AFM) magnetic coupling. A gradual AFM/FM crossover with the number of ML is particularly appealing for studies of the competition of magnetic states. Magnetic metalloxenes, a family of layered materials REX_2 formed by rare earths (RE = Eu or Gd) and 2D-Xenes (graphene analogues, silicene or germanene),[8,9,30] demonstrate such evolution of the magnetic state. A major

[1] *Department of Physics & Swiss Nanoscience Institute, University of Basel, 4056 Basel, Switzerland.*
[2] *Department of Physics and Astronomy & Institute for Quantum Computing, University of Waterloo, Waterloo, ON N2L 3G1, Canada*
[3] *National Research Center "Kurchatov Institute", Kurchatov Sq. 1, 123182 Moscow, Russia.*
[§] Contributed equally to this work
[#] Current affiliation: *National Research Council, Ottawa, ON K1A 0R6, Canada*
E-mail: martino.poggio@unibas.ch (MP), vgstorchak9@gmail.com (VGS)
Electronic Supplementary Information (ESI) available. See
DOI: 10.1039/x0xx00000x

Please do not adjust margins

outcome of the AFM/FM competition in these systems is that the gradually changing FM moment does not reach the value expected for full spin polarization (7 μ_B per Eu or Gd ion), even in the monolayer limit. The most compelling evidence of the coexistence of AFM and FM phases is the observation of intrinsic exchange bias (EB) in $GdSi_2$,[31] $EuSi_2$ and $EuGe_2$.[32] In the metalloxenes, the EB effect is an emerging property; it manifests itself in films of several ML thickness.[31,32] Although the REX_2 films exhibiting EB are only several ML thick their magnetism is yet of 3D nature (see below). However, the magnetic response of REX_2 to high magnetic fields studied by X-ray magnetic circular dichroism[33] supports the idea that the AFM/FM competition extends to monolayer metalloxenes. Further evidence and analysis are necessary to validate the phase-separated state in the 2D limit. This knowledge is indispensable in establishing 2D magnets as prospective materials for ultra-compact spintronics.

Theoretical approach to the AFM/FM competition in REX_2 is problematic: the elaborate calculations of RE metalloxenes[34-37] fail to confirm the sharp fall-off in the magnetic moment in the 2D materials. So far, the experimental evidence of the AFM/FM competition is circumstantial. Direct visualization would be most informative. What we need is to choose the visualization technique and the material for the study. On the one hand, scanning tunnelling microscopy has been applied to Cr-based 2D magnets, to explore the layer-dependent magnetism in $CrBr_3$ down to a single monolayer,[38,39] the AFM order in 1 ML $CrTe_2$,[40] the AFM-to-FM transition in few-layer CrI_3.[41] On the other hand, nanoscale magnetic imaging techniques are natural candidates to probe the spatial variation of order parameters in 2D systems due to advantageous combination of high spatial resolution and high magnetic field sensitivity.[42] Such techniques have been successfully applied to 2D and layered nanosystems: scanning SQUID microscopy – to describe FM in twisted bilayer graphene,[43] single-spin microscopy – to probe magnetism in 2D CrI_3[44] and $CrBr_3$,[45] magnetic force microscopy (MFM) – to study the magnetic structures of the Fe_3GaTe_2[46] and Cr_5Te_8[47] nanosheets. Our choice here is MFM, a technique that has proven itself in studies of coexisting magnetic orders, arising due to stacking variations in a flake of CrI_3[48] or due to the AFM-to-FM transition in few ML of CrSBr.[49] We note that the inhomogeneity in CrI_3 is probed in rather thick flakes (thickness from dozens to hundreds of nm)[48] while in CrSBr it is limited to a transient state at T_N.[49] In contrast, here we raise the question of the magnetic homogeneity of the ground state in 2D materials at the monolayer limit.

So far, the MFM studies of 2D materials have been limited to 3*d* magnets; information on the spatial distribution of magnetic orders in 4*f* 2D magnets being rather limited. As for material, we focus our attention on the germanene-based 4*f* metalloxene $EuGe_2$[9,50] because of its structural stability: the material does not suffer from any significant amount of anionic vacancies as GdX_2[9] or pseudomorphism as $EuSi_2$.[51] The thickness of 2 ML $EuGe_2$ is deemed optimal for the study because it avoids the dominance of the FM state as in the $EuGe_2$ monolayer; yet the magnetism of the bilayer is of 2D nature, as demonstrated below.

Here, we report synthesis of the epitaxial film of 2 ML $EuGe_2$ on Ge, its structural and magnetic characterization. The spatial distribution of the magnetic states in this 2D magnet is probed employing a high-sensitivity MFM technique. We demonstrate an inhomogeneous magnetic ground state and map its evolution with temperature and magnetic field.

Results and discussion

Synthesis and characterization of $EuGe_2$ bilayer

The germanene-based trigonal polymorph of $EuGe_2$ (Fig. 1a) is stable and even established as a phase prototype. However, its synthesis is not a trivial matter. Production of bulk $EuGe_2$ by heating elemental Eu and Ge in a crucible suffers from the formation of the side product Eu_3Ge_5.[52] To avoid this problem, we synthesize $EuGe_2$ layer-by-layer employing molecular beam epitaxy (MBE). The synthesis proceeds *via* reaction of deposited Eu with the Ge substrate serving as a reactant. MFM measurements pose certain requirements to the surface of the sample. Because a uniformly magnetized magnetic film produces no stray field, finite 2D geometries are required for magnetic imaging techniques to discern a uniformly magnetized material *via* the edge fields it produces. Therefore, the pristine Ge surface was patterned to produce raised 2D structures (with a typical height of about 0.5 μm) of different form. The virtually unlimited supply of Ge from the substrate prevents formation of Ge-deficient Eu_3Ge_5. Also, the substrate controls the orientation of the layered $EuGe_2$ structure. We employ the Ge(111) face of the substrate because its topmost layer matches structurally the honeycomb germanene layer of $EuGe_2$. This lattice match stabilizes the orientation of the $EuGe_2$ layers parallel to the surface. $EuGe_2$ on Ge(111) is produced in rather mild conditions. The material is susceptible to oxidation by air. Therefore, the film is capped with a layer of amorphous non-magnetic SiO_x to avoid its partial oxidation during *ex situ* experiments.

The structural quality of the material has been attested by a combination of techniques. Fig. 1b demonstrates the microstructure of the $EuGe_2$ bilayer on Ge(111) imaged by scanning transmission electron microscopy (STEM) in the high-angle annular dark field (HAADF) mode. Each monolayer is formed by a flat layer of Eu and a buckled layer of germanene, in agreement with the ball-and-stick presentation in Fig. 1a. Reflection high-energy electron diffraction (RHEED) characterizes the 2 ML film *in situ*. The system of the RHEED reflexes (Fig. 1c) agrees with the structure of trigonal $EuGe_2$ with the layers oriented parallel to the film surface. This conclusion is confirmed by X-ray diffraction (XRD); a typical θ-2θ XRD scan (Fig. 1d) demonstrates reflexes of $EuGe_2$ and the substrate only, without any traces of other phases. RHEED and XRD determine the lattice parameters of 2 ML $EuGe_2$: a = 4.04(5) Å and c = 5.116(11) Å. The parameters can be compared with those determined in thick $EuGe_2$ films (a = 4.11(3) Å and c = 4.9853(9) Å)[50] and bulk $EuGe_2$

 This journal is © The Royal Society of Chemistry 20xx

(a = 4.10095(32) Å and c = 4.99811(44) Å).[52] The difference is rather significant; it is likely to be explained by strong influence of the adjacent Ge substrate on the ultrathin film (the parameter a of 2 ML $EuGe_2$ falls between those of Ge and bulk $EuGe_2$).

The large area of the synthesized samples provides an opportunity to study the magnetic properties of $EuGe_2$ employing a SQUID magnetometer. $EuGe_2$ exhibits easy-plane magnetism.[9,50] Fig. 2a presents temperature dependence of the FM moment in 2 ML $EuGe_2$ in different in-plane magnetic fields, revealing a strong dependence of the effective transition temperature on weak magnetic fields. This feature, caused by magnetic field dependence of the (pseudo)gap opening in the spin-wave spectrum,[53] is a hallmark of 2D magnetism, observed in studies of $Cr_2Ge_2Te_6$[5] and RE metalloxenes.[8,9,30] The sample exhibits other properties typical of FM materials such as bifurcation of field-cooled and zero-field-cooled magnetization. The M-H curves (Fig. 2b) demonstrate a hysteresis loop (this property is lost in 1 ML $EuGe_2$ putting forward another argument in favour of 2 ML $EuGe_2$ for the MFM study). Even at low temperature, the hysteresis loop differs from that in a canonical FM material. Instead, it resembles a double hysteresis loop, indicating a complex magnetic structure. At T = 2 K, H_c is about 150 Oe. At higher temperature, the loop shrinks and H_c becomes negligible, within the experimental error. The remanence at 2 K corresponds to the magnetic moment of about 0.35 μ_B/Eu or, equivalently, 4.9 μ_B/nm^2; the saturation magnetic moments are about 1.0 μ_B/Eu at 2 K, 0.6 μ_B/Eu at 5 K, and 0.4 μ_B/Eu at 15 K. The saturation moment at low temperature is well below 7 μ_B/Eu, the value expected for the half-filled 4f-shells of Eu^{2+} ions (the neutron diffraction studies of bulk $EuGe_2$ determine the magnetic moments of Eu to be 7.1(2) μ_B/Eu).[54] This is a key observation because it points at the presence of other magnetic phases. It should be noticed here that reduction of Eu magnetic moments in 2D magnets is found in other compounds as well, $EuSi_2$,[8] EuC_6[55] and Eu superstructures on Si(001).[56]

Detailed calculations of ultrathin $EuGe_2$ have been reported recently.[34] The calculations have been carried out for 4 different magnetic configurations. Unfortunately, the results of the calculations do not capture the salient features of the experiment such as the competition between magnetic states and the easy-plane magnetic anisotropy. The problem turns out to be rather general: calculations of other 2D magnetic metalloxenes with $4f^7$ cations do not reproduce the competition of magnetic states as well. It applies to $EuSi_2$,[35] $GdSi_2$,[36] and $GdGe_2$[37] – strongly correlated materials with the same structure as that of $EuGe_2$. This systematic failure calls for significant advances in the computational methodology. The energies of the FM and AFM states are probably not much different in Eu lattices. Take for example $EuCd_2As_2$, a material with triangular Eu layers: its AFM/FM transition is driven by low pressure;[57] the magnetic order can be controlled by the level of band filling.[58] Although the SQUID measurements have provided the basic picture of $EuGe_2$ magnetism, the standard SQUID is not the best technique to probe competing states because it does not provide spatially resolved information; therefore, other techniques (such as MFM) are required to characterize the peculiar magnetism of 2 ML $EuGe_2$.

Magnetic force microscopy of $EuGe_2$ bilayer

Field-dependent edge scans

To image 2 ML $EuGe_2$, we carry out an MFM study using a magnet-tipped nanowire (NW) as the scanning probe.[59] Such NW MFM probes are ideal for imaging weak magnetic field patterns on the nanometer-scale[42] because of their tiny magnetic tips, which are grown by focused-electron-beam-induced deposition of Co,[60] and the NWs' high-force sensitivity.[61] The investigated sample consists of a patterned array of elevated micron-scale mesas, on which 2 ML of $EuGe_2$ have been grown by MBE. The elevated structures give the 2D magnetic system well-defined edges that produce stray magnetic field for our scanning probe to image. The array is mounted in high vacuum inside a custom NW scanning probe microscope and cooled down to liquid helium temperature.

In order to demonstrate the technique's sensitivity to the weak stray fields produced by $EuGe_2$, we first image the sample *via* MFM as a function of the applied out-of-plane magnetic field B. In particular, we map the frequency shift produced by the tip-sample interaction above a region of the sample, which has been patterned in the shape of a rectangular bar, as shown in Fig. 3a. The MFM images are taken at T = 4.7 K for a series of magnetic fields ranging from 0.1 T to 8 T. Fig. 4a shows frequency maps at a tip-sample distance of d = 210 nm. During a scan, we record the frequency shift of both of the NW's flexural modes, $\Delta f_1 = f_1 - f_{0,1}$ and $\Delta f_2 = f_2 - f_{0,2}$, as well as their oscillation amplitudes R_1 and R_2. $f_{0,1}$ and $f_{0,2}$ are the natural resonance frequencies of the modes in the absence of interaction with the sample. The quantity displayed in the images is the frequency shift of both modes defined as $\Delta f = \Delta f_1 + \Delta f_2$ which combines the signals originating from the two orthogonal mode directions, each of which – in the limit of a strongly magnetized sample (see Note S1, ESI) – is proportional to the spatial derivative of the sample's in-plane stray magnetic field taken along each of the NW mode directions: $\Delta f_{1,2} \propto dB_{x1,2}/dx_{1,2}$.

As a function of increasing applied field B, Δf emerges and intensifies at the edges of the bar structure. Note that the second row of images in Fig. 4a uses a scale that is four times larger than the first row. As the probe crosses an edge onto $EuGe_2$ from any direction, we first observe a dip followed by a peak in the mean frequency shift, just as expected from a magnet that is uniformly polarized in the out-of-plane direction. In order to analyse this data, we take line-cuts of Δf_1 for each image in Fig. 4a along the axis x_{rot}. We then average the data along the axis parallel to the border (perpendicular to x_{rot}), producing the plot shown in Fig. 4b. We select the first NW mode because its oscillation direction is nearly perpendicular to the long edge of the bar, therefore providing a high imaging contrast across this boundary.

In order to quantify the magnitude of the in-plane stray field at the edge of the structure, we approximate our MFM tip

as a magnetic monopole and apply the tip transfer function approach,[62,63] in which the frequency shift and magnetic field are related in the one-dimensional Fourier space by

$$\hat{B}_1(k) = i\frac{k_1}{\pi q_0 f_1 k}\widehat{\Delta f}_1(k)$$

where k_1 is the spring constant of the first mode, q_0 the magnetic surface charge, $\hat{B}_1(k)$ and $\widehat{\Delta f}_1(k)$ the Fourier transforms of field and frequency shift and k the wave vector. Transforming the field back to real space, taking the peak values of the resulting line cuts, and plotting them against the external field gives the curve shown in Fig. 4c. In a few fields, a systematic deviation of the edge field values for all distances stands out. These deviations result from the uncertainty of the "soft touch" calibration procedure, which can lead to errors in the tip-sample distance calibration of up to 10 nm and becomes less accurate in higher applied fields. Nevertheless, the increasing out-of-plane field at the sample edge as a function of B is consistent with a gradual alignment of the $EuGe_2$ magnetization along the out-of-plane direction, saturating just above B = 2 T. Furthermore, the images in large B match the pattern that is expected for a fully out-of-plane magnetized sample from simulations (see Note S1, ESI). We find no evidence of magnetic hysteresis for out-of-plane applied field, as expected for an in-plane AFM/FM material. Unfortunately, due to the probe design, we are not able to apply in-plane magnetic fields, for which hysteresis is expected (Fig. 2b).

Temperature-dependent transition

In order to investigate the sample's magnetic phase transition, we carry out NW MFM at different temperatures. As shown in Fig. 5, we image the same region of the sample as in Fig. 4 in the absence of an applied magnetic field (B = 0 T) and at a tip-sample distance d = 100 nm. The top row shows images of Δf, while the bottom row shows changes in the dissipation $\Delta\Gamma$, which is the mean of the dissipations of both modes $\Delta\Gamma = (\Delta\Gamma_1 + \Delta\Gamma_2)/2$. The individual changes in dissipation are computed from the corresponding oscillation amplitude *via* $\Delta\Gamma_i \approx \Gamma_{0,i}(R_{0,i}/R_i - 1)$, $(i = 1,2)$, where $\Gamma_{0,i} = m_{eff}\,\omega_{0,i}/Q_{0,i}$, m_{eff} is the motional mass, $\omega_{0,i}$ the angular resonance frequency, and $Q_{0,i}$ the quality factor of the ith mode. The approximation assumes that the frequency shifts are small compared to the absolute resonance frequencies, which is the case in this experiment.

Above T = 20 K, the images of Δf show a non-magnetic contrast related to the tip-sample force gradients resulting from electro-static interactions with the sample and reflecting its topography. Below around 15 K, a granular structure starts to appear above the rectangular mesa. This contrast increases in intensity as the temperature is decreased further. The average Δf reaches a maximum at 6.8 K, before decreasing to a lower value at the base temperature of 4.7 K. Fig. 5c shows the overall behaviour of the frequency shift Δf_{avg} as a function of temperature, where Δf_{avg} is Δf averaged over the rectangular mesa as indicated by the dotted lines in Fig. 5a.

The corresponding images of the dissipation $\Delta\Gamma$ are shown in Fig. 5b. Above T = 15 K, there is no sign of dissipation above the mesa. Below 13 K, however, elongated regions on the order of a few hundred nanometers in length and tens of nanometers in width begin to appear. These features grow denser and more pronounced with decreasing temperature down to a maximum in the average dissipation at 9.8 K. Further reduction of temperature down to 4.7 K results in a drop in the overall dissipation contrast. Fig. 5d shows $\Delta\Gamma_{avg}$ as a function of temperature, where $\Delta\Gamma_{avg}$ is $\Delta\Gamma$ averaged over the rectangular mesa as indicated by the dotted lines in Fig. 5b.

While both Δf and $\Delta\Gamma$ maps show a strong spatial dependence of the magnitudes of both the frequency shift and the dissipation with a wide range of characteristic length-scales in the hundreds of nm, detailed analysis shows no significant variation of the local temperature dependence of Δf and $\Delta\Gamma$. Even when integrating over regions of the sample on the scale of 100 nm, Δf and $\Delta\Gamma$ continue to show peaks in their temperature dependence around 6.8 and 9.8 K respectively.

In the absence of an applied magnetic field, as in the measurements shown in Fig. 5, the stray field of the NW MFM tip, which can be up to tens of mT along the NW long axis at this tip-sample distance, locally magnetizes the sample underneath. As a result, rather than revealing the $EuGe_2$ sample's stray magnetic field gradient, Δf is proportional to the local in-phase magnetic susceptibility χ' and $\Delta\Gamma$ to the out-of-phase susceptibility χ'' (see Note S1, ESI). This interpretation is confirmed by the observation that switching the magnetization of the NW MFM tip does not invert the frequency shift contrast, as would be expected if Δf were determined by the sample's stray magnetic field (see Fig. S1, ESI). The resulting images show the spatial variation of both χ', which indicates the linear response of the sample magnetization to a change in the local tip field, and χ'', which is related to dissipative processes in the sample magnetization caused by the moving magnetic tip. Both of these quantities are sensitive to thermodynamic phase changes and sharp features in their temperature-dependence point to a magnetic phase transition. Transition temperatures between 6 and 10 K in Δf and $\Delta\Gamma$ are consistent with the temperature-dependence of the FM moment measured for 2 ML $EuGe_2$ and shown in Fig. 2a, if we assume that the NW MFM tip produces a few mT of in-plane field in the sample.

The spatial inhomogeneity present in both the Δf and $\Delta\Gamma$ images indicates the presence of magnetic domains. Different magnetic phases, *e.g.* AFM and FM, are expected to produce χ' and χ'' responses of different magnitudes, which could be responsible for the observed local variations in Δf and $\Delta\Gamma$ near the magnetic transition. Given the wide range of characteristic length scales observed, the measurements suggest AFM/FM domains with characteristic sizes in the hundreds of nm (Note S2 and Fig. S2, ESI). Up to date, two basic models of magnetic phase separation have been developed, one related to charge segregation and one that is electroneutral.[17] The domain size for charge segregation is driven by the competition between the exchange and Coulomb contributions and, therefore,

 This journal is © The Royal Society of Chemistry 20xx

expected to be rather small, on the order of a nanometer.[17] In contrast, the second type can furnish domains of a much larger size. Experimental observation of this type of magnetic phase separation is well documented: magnetic domains extending to several hundreds of nm have been detected in manganites.[64-67] The domain size in the ground state of the 2D magnet $EuGe_2$ is of the same order of magnitude. The large magnetic domains observed in the MFM experiments support the model based on electroneutral phase separation rather than charge segregation. However, this support for the model, based on the size of magnetic domains, is circumstantial. Although the presented results are highly suggestive, direct experimental evidence of electroneutrality is still lacking.

Conclusions

The emerging field of 2D magnetism offers enormous opportunities in studies of magnetic phases and their competition. In particular, the interplay between FM and AFM states plays a significant role in the world of 2D magnets, observed in a number of materials and expected to be a basis for spintronic applications. Our aim here was to get insight into the structure of the phase-separated state, *i.e.* a state where both FM and AFM domains coexist. Two crucial elements of the endeavour were the choice of the material and the choice of the experimental technique. Among the 2D magnets, germanene-based $EuGe_2$ was taken because of its dimensional AFM-to-FM crossover, established with the help of magnetization and electron transport measurements. The presence of the phase-separated state followed from reduced magnetic moments in the ground state and the intrinsic exchange bias effect but direct observation of the magnetic state was lacking. To fill the gap, the present study employed MFM, a technique proven successful in studies of both 2D magnets and phase separation. Mapping of the magnetic state of the $EuGe_2$ bilayer across its magnetic transition demonstrated appearance of a grainy magnetic structure expected for a phase-separated state. A key result is the determination of the characteristic sizes of the magnetic domains amounting to several hundreds of nm. The size of the domains in the 2D magnet agrees with those at the surfaces of 3D materials in a magnetic-phase-separated state, underscoring the similarity between the phenomena. The study can be extended to other 2D magnets with presumed coexistence of magnetic states. We expect the present work to provide a platform for nanoscale magnetic field imaging in various 2D materials at the monolayer limit.

Experimental

Synthesis

The $EuGe_2$ film was synthesized in a Riber Compact system for molecular beam epitaxy. The synthesis was carried out under ultra-high vacuum (base pressure below 10^{-10} Torr) conditions. The substrate for the synthesis was a Ge wafer with a lateral size of 1 inch. The (111) face of Ge stabilized the layered structure of the film; the miscut angle did not exceed 0.5°. The Ge wafer surface was patterned to produce a set of elevated micron-sized mesas of different shapes. Then, the natural oxide on the Ge surface was removed by annealing the wafer at 650 °C. The substrate temperature was determined by a thermocouple and a PhotriX ML-AAPX/090 infrared pyrometer operating at a wavelength 0.9 µm. 4N Eu was supplied from a Knudsen cell effusion source heated up to 400 °C; the corresponding pressure P_{Eu} was 10^{-8} Torr, according to a Bayard-Alpert ionization gauge fitted at the substrate site. The $EuGe_2$ bilayer was produced by reaction of Eu with the Ge(111) substrate at 290 °C. To avoid degradation by air, $EuGe_2$ was capped with a 20-nm protective layer of amorphous SiO_x deposited at room temperature.

Characterization

The structure of the $EuGe_2$ film was analyzed by a combination of diffraction and microscopy techniques. The surfaces of the substrate and the film were probed in the MBE growth chamber employing a RHEED diffractometer furnished with the kSA 400 analytical RHEED system. The other studies were carried out *ex situ*. The θ-2θ XRD scan was produced in a Rigaku SmartLab 9 kW diffractometer employing a $CuK_{\alpha 1}$ source. The spectrum was recorded in the high-resolution mode ($\Delta q_z \approx 0.0004$ Å^{-1}) using a double-bounce monochromator Ge (220) (+−), a collimating parabolic mirror, and a system of collimating slits. A cross-sectional specimen of 2 ML $EuGe_2$ for electron microscopy studies was prepared in a Helios NanoLab 600i scanning electron microscope/focused ion beam (FIB) dual beam system. The film was capped with a 2 µm layer of Pt. Then, a membrane with dimensions 2 µm × 5 µm × 5 µm was cut by FIB milling with 30 keV Ga^+ ions, thinned and cleaned to electron transparency with 5 and 2 keV Ga^+ ions. The specimen was imaged in a TEM/STEM Cs probe corrected microscope Titan 80-300 employing the HAADF mode. Digital Micrograph and Tecnai Imaging and Analysis software packages were used to process the images.

The magnetic properties of the $EuGe_2$ film were determined by an MPMS XL-7 SQUID magnetometer. The sample (5 mm × 5 mm) was mounted in a plastic straw and oriented with respect to the external magnetic field with an accuracy of better than 2°. The measurements were carried our employing the reciprocating sample option. The FM moments in the $EuGe_2$ film were determined by subtraction of the diamagnetic signal of the Ge substrate (measured in a separate experiment). An alternative estimate of the FM moments by subtraction of contributions linear in magnetic field (see Ref. 8) provided close results, certifying their consistency.

Magnetic force microscopy

Nanowire force microscopy utilizes a NW resonator in the pendulum geometry as a universal scanning probe for measuring in-plane force gradients along the oscillation

directions of the two first-order flexural modes.[68,69] Magnetic imaging contrast is achieved by either preparing a magnet at the end of the NW[56] or using a fully magnetic resonator.[57] In this work, the former approach was employed. The readout of the NW's motion was carried out optically using a fiber-based interferometer. Our custom-built NW scanning probe microscope is described in detail in Refs. 59 and 60.

To increase the sensitivity and robustness of NW MFM, the magnetic scanning probe consisted of a high-quality Si NW[61] equipped with a magnetic cobalt tip grown by focused electron beam induced deposition (FEBID).[70] A scanning electron microscope image of the full NW and a close up of its tip are shown in Figs. 3b and 3c and the cobalt part is artificially highlighted in blue. From the images we extract the length without the tip of the NW probe selected for this study to be l = 21 nm. The tip itself is anchored to the side of the droplet at the free NW end and continued to grow vertically in parallel to the NW-axis adding roughly 700 nm to the overall length of the NW. Its diameter expands from 80 nm to 150 nm at the very end forming an elongated drop-like shaped object. The tip-sample distance was calibrated using a "soft touch" to the sample surface.

The NW's resonance frequencies and effective mass at a temperature of T_{NW} = 11 K and zero applied magnetic field are, as inferred from thermal noise spectra, $f_{0,1} \simeq$ 353.6 kHz, $f_{0,2} \simeq$ 355.5 kHz, and $m_{eff} = 3.2 \times 10^{-16}$ kg with a quality factor of $Q \simeq 19 \times 10^3$. This leads to thermally limited force sensitivity at resonance of $F_{min} \simeq 4.8$ aN Hz$^{-1/2}$. Transforming this value into a field sensitivity by applying the magnetic monopole model[60,62,71] for the tip-sample interaction with a value for the magnetic surface charge of $q_0 \simeq 3.0 \times 10^{-9}$ Am yields a thermally limited field sensitivity of $B_{min} \simeq 1.6$ nT Hz$^{-1/2}$.

The second batch of measurements was designed to investigate the temperature dependence of the $EuGe_2$ magnetization. Staying at zero field for the complete series and starting out at elevated temperatures of slightly above T = 30 K, the sample temperature was continuously lowered down to base temperature. At every temperature, the tip-sample distance and the scanning range were carefully calibrated. As with the first set of measurements the end section of the bar structure was imaged for a few different tip-sample distances ranging from 80 nm to 110 nm.

Author Contributions

Hinrich Mattiat: Investigation, Writing – original draft. **Lukas Schneider:** Investigation, Writing – original draft. **Patrick Reiser:** Investigation. **Martino Poggio:** Investigation, Writing – original draft, Supervision. **Pardis Sahafi:** Investigation. **Andrew Jordan:** Investigation. **Raffi Budakian:** Investigation. **Dmitry V. Averyanov:** Investigation. **Ivan S. Sokolov:** Investigation. **Alexander N. Taldenkov:** Investigation. **Oleg E. Parfenov:** Investigation. **Oleg A. Kondratev:** Investigation. **Andrey M. Tokmachev:** Writing – original draft. **Vyacheslav G. Storchak:** Investigation, Writing – original draft, Supervision.

Conflicts of interest

There are no conflicts to declare.

Acknowledgments

This work is supported by NRC "Kurchatov Institute", the Ministry of Science and Higher Education of Russia (Agreement No. 075-15-2021-1351), and the Russian Science Foundation [grants 22-13-00004 (synthesis), 19-19-00009 (magnetism studies), and 20-79-10028 (structural characterization)]. D.V.A. acknowledges support from the President's scholarship (SP 3111.2022.5). Part of the work has been carried out using the equipment of the resource centers of electrophysical, electron microscopy, and laboratory X-ray techniques at NRC "Kurchatov Institute". We acknowledge the support of the Canton Aargau, the Swiss National Science Foundation via Project Grant No. 200020-178863, and the Swiss Nanoscience Institute via Ph.D. Project P1905. This work was supported in part *via* funding from the US Army Research Office through Grant W911NF1610199, the Canada First Research Excellence Fund (CFREF), and the Natural Sciences and Engineering Research Council of Canada. The University of Waterloo's Quantum-Nano Fabrication and Characterization Facility (QNFCF) was used for this work. This infrastructure would not be possible without the significant contributions of Transformative Quantum Technologies (CFREF-TQT), Canada Foundation for Innovation (CFI), Industry Canada, the Ontario Ministry of Research and Innovation, and Mike and Ophelia Lazaridis.

References

1 C. Gong and X. Zhang, *Science*, 2019, **363**, eaav4450.
2 M. Gibertini, M. Koperski, A. F. Morpurgo and K. S. Novoselov, *Nat. Nanotechnol.*, 2019, **14**, 408-419.
3 B. Huang, M. A. McGuire, A. F. May, D. Xiao, P. Jarillo-Herrero and X. Xu, *Nat. Mater.*, 2020, **19**, 1276-1289.
4 H. Kurebayashi, J. H. Garcia, S. Khan, J. Sinova and S. Roche, *Nat. Rev. Phys.*, 2022, **4**, 150-166.
5 C. Gong, L. Li, Z. Li, H. Ji, A. Stern, Y. Xia, T. Cao, W. Bao, C. Wang, Y. Wang, Z. Q. Qiu, R. J. Cava, S. G. Louie, J. Xia and X. Zhang, *Nature*, 2017, **546**, 265-269.
6 B. Huang, G. Clark, E. Navarro-Moratalla, D. R. Klein, R. Cheng, K. L. Seyler, D. Zhong, E. Schmidgall, M. A. McGuire, D. H. Cobden, W. Yao, D. Xiao, P. Jarillo-Herrero and X. Xu, *Nature*, 2017, **546**, 270-273.
7 A. P. Balan, S. Radhakrishnan, C. F. Woellner, S. K. Sinha, L. Deng, C. de los Reyes, B. M. Rao, M. Paulose, R. Neupane, A. Apte, V. Kochat, R. Vajtai, A. R. Harutyunyan, C.-W. Chu, G. Costin, D. S. Galvao, A. A. Martí, P. A. van Aken, O. K. Varghese, C. S. Tiwary, A. M. M. R. Iyer and P. M. Ajayan, *Nat. Nanotechnol.*, 2018, **13**, 602-609.
8 A. M. Tokmachev, D. V. Averyanov, O. E. Parfenov, A. N. Taldenkov, I. A. Karateev, I. S. Sokolov, O. A. Kondratev and V. G. Storchak, *Nat. Commun.*, 2018, **9**, 1672.
9 A. M. Tokmachev, D. V. Averyanov, A. N. Taldenkov, O. E. Parfenov, I. A. Karateev, I. S. Sokolov and V. G. Storchak, *Mater. Horiz.*, 2019, **6**, 1488-1496.

 This journal is © The Royal Society of Chemistry 20xx

10 A. L. Sharpe, E. J. Fox, A. W. Barnard, J. Finney, K. Watanabe, T. Taniguchi, M. A. Kastner and D. Goldhaber-Gordon, *Science*, 2019, **365**, 605-608.
11 J. Su, P. Lyu and J. Lu, *Precis. Chem.*, 2023, **1**, 565.
12 K. F. Mak, J. Shan and D. C. Ralph, *Nat. Rev. Phys.*, 2019, **1**, 646-661.
13 T. Li, S. Jiang, N. Sivadas, Z. Wang, Y. Xu, D. Weber, J. E. Goldberger, K. Watanabe, T. Taniguchi, C. J. Fennie, K. F. Mak and J. Shan, *Nat. Mater.*, 2019, **18**, 1303-1308.
14 B. Huang, G. Clark, D. R. Klein, D. MacNeill, E. Navarro-Moratalla, K. L. Seyler, N. Wilson, M. A. McGuire, D. H. Cobden, D. Xiao, W. Yao, P. Jarillo-Herrero and X. Xu, *Nat. Nanotechnol.*, 2018, **13**, 544-548.
15 T. Song, X. Cai, M. W.-Y. Tu, X. Zhang, B. Huang, N. P. Wilson, K. L. Seyler, L. Zhu, T. Taniguchi, K. Watanabe, M. A. McGuire, D. H. Cobden, D. Xiao, W. Yao and X. Xu, *Science*, 2018, **360**, 1214-1218.
16 O. E. Parfenov, A. M. Tokmachev, D. V. Averyanov, I. A. Karateev, I. S. Sokolov, A. N. Taldenkov and V. G. Storchak, *Mater. Today*, 2019, **29**, 20-25.
17 E. Dagotto, T. Hotta and A. Moreo, *Phys. Rep.*, 2001, **344**, 1-153.
18 V. G. Storchak, D. G. Eshchenko, E. Morenzoni, T. Prokscha, A. Suter, X. Liu and J. K. Furdyna, *Phys. Rev. Lett.*, 2008, **101**, 027202.
19 Z. Li, X. Zhang, X. Zhao, J. Li, T. S. Herng, H. Xu, F. Lin, P. Lyu, X. Peng, W. Yu, X. Hai, C. Chen, H. Yang, J. Martin, J. Lu, X. Luo, A. H. Castro Neto, S. J. Pennycook, J. Ding, Y. Feng and J. Lu, *Adv. Mater.*, 2020, **32**, 1907645.
20 T. Song, Q.-C. Sun, E. Anderson, C. Wang, J. Qian, T. Taniguchi, K. Watanabe, M. A. McGuire, R. Stöhr, D. Xiao, T. Cao, J. Wrachtrup and X. Xu, *Science*, 2021, **374**, 1140-1144.
21 Y. Xu, A. Ray, Y.-T. Shao, S. Jiang, K. Lee, D. Weber, J. E. Goldberger, K. Watanabe, T. Taniguchi, D. A. Muller, K. F. Mak and J. Shan, *Nat. Nanotechnol.*, 2022, **17**, 143-147.
22 G. Zheng, W.-Q. Xie, S. Albarakati, M. Algarni, C. Tan, Y. Wang, J. Peng, J. Partridge, L. Farrar, J. Yi, Y. Xiong, M. Tian, Y.-J. Zhao and L. Wang, *Phys. Rev. Lett.*, 2020, **125**, 047202.
23 C. Wang, J. Wang, W.-Q. Xie, G. Zhang, H. Wu, J. Zhou, X. Zhu, W. Ning, G. Wang, C. Tan, L. Wang, H. Du, Y.-J. Zhao, H. Chang, G. Zheng, W.-T. Geng and M. Tian, *Phys. Rev. B*, 2023, **107**, L140409.
24 T. Song, Z. Fei, M. Yankowitz, Z. Lin, Q. Jiang, K. Hwangbo, Q. Zhang, B. Sun, T. Taniguchi, K. Watanabe, M. A. McGuire, D. Graf, T. Cao, J.-H. Chu, D. H. Cobden, C. R. Dean, D. Xiao and X. Xu, *Nat. Mater.*, 2019, **18**, 1298-1302.
25 C. X. Trang, Q. Li, Y. Yin, J. Hwang, G. Akhgar, I. Di Bernardo, A. Grubišić-Čabo, A. Tadich, M. S. Fuhrer, S.-K. Mo, N. V. Medhekar and M. T. Edmonds, *ACS Nano*, 2021, **15**, 13444-13452.
26 Z. Zang, M. Xi, S. Tian, R. Guzman, T. Wang, W. Zhou, H. Lei, Y. Huang and Y. Ye, *ACS Appl. Electron. Mater.*, 2022, **4**, 3256-3262.
27 A. Bedoya-Pinto, J.-R. Ji, A. K. Pandeya, P. Gargiani, M. Valvidares, P. Sessi, J. M. Taylor, F. Radu, K. Chang and S. S. P. Parkin, *Science*, 2021, **374**, 616-620.
28 E. J. Telford, A. H. Dismukes, R. L. Dudley, R. A. Wiscons, K. Lee, D. G. Chica, M. E. Ziebel, M.-G. Han, J. Yu, S. Shabani, A. Scheie, K. Watanabe, T. Taniguchi, D. Xiao, Y. Zhu, A. N. Pasupathy, C. Nuckolls, X. Zhu, C. R. Dean and X. Roy, *Nat. Mater.*, 2022, **21**, 754-760.
29 J. Wang, L. Ma, X. Wang, X. Wang, J. Yao, Q. Yi, R. Tang and G. Zou, *Angew. Chem. Int. Ed.*, 2021, **133**, 25224-25231.
30 A. M. Tokmachev, D. V. Averyanov, I. S. Sokolov, A. N. Taldenkov, O. E. Parfenov, I. A. Karateev and V. G. Storchak, in Xenes: 2D Synthetic Materials beyond Graphene, (Eds: A. Molle and C. Grazianetti), Woodhead Publishing (Elsevier), Cambridge, US; 2022, Ch. 14, pp. 353-375.
31 D. V. Averyanov, I. S. Sokolov, A. N. Taldenkov, O. E. Parfenov, I. A. Karateev, O. A. Kondratev, A. M. Tokmachev and V. G. Storchak, *ACS Nano*, 2022, **16**, 19482-19490.
32 D. V. Averyanov, I. S. Sokolov, A. N. Taldenkov, O. E. Parfenov, I. A. Karateev, O. A. Kondratev, A. M. Tokmachev and V. G. Storchak, *Nanoscale Horiz.*, 2023, **8**, 803-811.
33 D. V. Averyanov, I. S. Sokolov, M. S. Platunov, F. Wilhelm, A. Rogalev, P. Gargiani, M. Valvidares, N. Jaouen, O. E. Parfenov, A. N. Taldenkov, I. A. Karateev, A. M. Tokmachev and V. G. Storchak, *Nano Research*, 2020, **13**, 3396-3402.
34 Z. Gao, Y. Wang, J. Gao, Z. Cui, X. Zhang, J. Shi and X. Fan, *Comp. Mater. Sci.*, 2022, **213**, 111611.
35 G. Yang, J.-S. Chai, K. Bu, L.-F. Xu and J.-T. Wang, *Phys. Chem. Chem. Phys.*, 2022, **24**, 6782-6787.
36 S. Demirci, T. Gorkan, Ş. Çallioğlu, Y. Yüksel, Ü. Akıncı, E. Aktürk and S. Ciraci, *Phys. Rev. B*, 2021, **104**, 224427.
37 Y. Wang, Z. Cui, H. Zeng, Z. Wang, X. Zhang, J. Shi, T. Cao and X. Fan, *J. Mater. Chem. C*, 2022, **10**, 1259-1269.
38 W. Chen, Z. Sun, Z. Wang, L. Gu, X. Xu, S. Wu and C. Gao, *Science*, 2019, **366**, 983-987.
39 P. Lyu, J. Sødequist, X. Sheng, Z. Qiu, A. Tadich, Q. Li, M. T. Edmonds, M. Zhao, J. Redondo, M. Švec, P. Song, T. Olsen and J. Lu, *ACS Nano*, 2023, **17**, 15441.
40 J.-J. Xian, C. Wang, J.-H. Nie, R. Li, M. Han, J. Lin, W.-H. Zhang, Z.-Y. Liu, Z.-M. Zhang, M.-P. Miao, Y. Yi, S. Wu, X. Chen, J. Han, Z. Xia, W. Ji and Y.-S. Fu, *Nat. Commun.*, 2022, **13**, 257.
41 Z. Qiu, M. Holwill, T. Olsen, P. Lyu, J. Li, H. Fang, H. Yang, M. Kashchenko, K. S. Novoselov and J. Lu, *Nat. Commun.*, 2021, **12**, 70.
42 E. Marchiori, L. Ceccarelli, N. Rossi, L. Lorenzelli, C. L. Degen and M. Poggio, *Nat. Rev. Phys.*, 2022, **4**, 49-60.
43 C. L. Tschirhart, M. Serlin, H. Polshyn, A. Shragai, Z. Xia, J. Zhu, Y. Zhang, K. Watanabe, T. Taniguchi, M. E. Huber and A. F. Young, *Science*, 2021, **372**, 1323-1327.
44 L. Thiel, Z. Wang, M. A. Tschudin, D. Rohner, I. Gutiérrez-Lezama, N. Ubrig, M. Gibertini, E. Giannini, A. F. Morpurgo and P. Maletinsky, *Science*, 2019, **364**, 973-976.
45 Q.-C. Sun, T. Song, E. Anderson, A. Brunner, J. Förster, T. Shalomayeva, T. Taniguchi, K. Watanabe, J. Gräfe, R. Stöhr, X. Xu and J. Wrachtrup, *Nat. Commun.*, 2021, **12**, 1989.
46 G. Zhang, F. Guo, H. Wu, X. Wen, L. Yang, W. Jin, W. Zhang and H. Chang, *Nat. Commun.*, 2022, **13**, 5067.
47 H. Wu, J. Guo, S. Zhaxi, H. Xu, S. Mi, L. Wang, S. Chen, R. Xu, W. Ji, F. Pang and Z. Cheng, *ACS Appl. Mater. Interfaces*, 2023, **15**, 26148-26158.
48 B. Niu, T. Su, B. A. Francisco, S. Ghosh, F. Kargar, X. Huang, M. Lohmann, J. Li, Y. Xu, T. Taniguchi, K. Watanabe, D. Wu, A. Balandin, J. Shi and Y.-T. Cui, *Nano Lett.*, 2020, **20**, 553-558.
49 D. J. Rizzo, A. S. McLeod, C. Carnahan, E. J. Telford, A. H. Dismukes, R. A. Wiscons, Y. Dong, C. Nuckolls, C. R. Dean, A. N. Pasupathy, X. Roy, D. Xiao and D. N. Basov, *Adv. Mater.*, 2022, **34**, 2201000.
50 O. E. Parfenov, D. V. Averyanov, A. M. Tokmachev, I. S. Sokolov, I. A. Karateev, A. N. Taldenkov and V. G. Storchak, *Adv. Funct. Mater.*, 2020, **30**, 1910643.
51 A. M. Tokmachev, D. V. Averyanov, I. A. Karateev, O. E. Parfenov, O. A. Kondratev, A. N. Taldenkov and V. G. Storchak, *Adv. Funct. Mater.*, 2017, **27**, 1606603.
52 N. D. Cultrara, Y. Wang, M. Q. Arguilla, M. R. Scudder, S. Jiang, W. Windl, S. Bobev and J. E. Goldberger, *Chem. Mater.*, 2018, **30**, 1335-1343.
53 P. Bruno, *Phys. Rev. B*, 1991, **43**, 6015-6021.
54 J. M. Cadogan, D. H. Ryan, R. Rejali and C. D. Boyer, *J. Alloys Compd.*, 2016, **688**, 51-54.
55 I. S. Sokolov, D. V. Averyanov, O. E. Parfenov, I. A. Karateev, A. N. Taldenkov, A. M. Tokmachev and V. G. Storchak, *Mater. Horiz.*, 2020, **7**, 1372-1378.

56 A. M. Tokmachev, D. V. Averyanov, A. N. Taldenkov, I. S. Sokolov, I. A. Karateev, O. E. Parfenov and V. G. Storchak, *ACS Nano*, 2021, **15**, 12034-12041.
57 E. Gati, S. L. Bud'ko, L.-L. Wang, A. Valadkhani, R. Gupta, B. Kuthanazhi, L. Xiang, J. M. Wilde, A. Sapkota, Z. Guguchia, R. Khasanov, R. Valentí and P. C. Canfield, *Phys. Rev. B*, 2021, **104**, 155124.
58 N. H. Jo, B. Kuthanazhi, Y. Wu, E. Timmons, T.-H. Kim, L. Zhou, L.-L. Wang, B. G. Ueland, A. Palasyuk, D. H. Ryan, R. J. McQueeney, K. Lee, B. Schrunk, A. A. Burkov, R. Prozorov, S. L. Bud'ko, A. Kaminski and P. C. Canfield, *Phys. Rev. B*, 2020, **101**, 140402(R).
59 N. Rossi, B. Gross, F. Dirnberger, D. Bougeard and M. Poggio, *Nano Lett.*, 2019, **19**, 930-936.
60 H. Mattiat, N. Rossi, B. Gross, J. Pablo-Navarro, C. Magén, R. Badea, J. Berezovsky, J. M. De Teresa and M. Poggio, *Phys. Rev. Appl.*, 2020, **13**, 044043.
61 P. Sahafi, W. Rose, A. Jordan, B. Yager, M. Piscitelli and R. Budakian, *Nano Lett.*, 2020, **20**, 218-223.
62 H. J. Hug, B. Stiefel, P. J. A. van Schendel, A. Moser, R. Hofer, S. Martin, H.-J. Güntherodt, S. Porthun, L. Abelmann, J. C. Lodder, G. Bochi and R. C. O'Handley, *J. Appl. Phys.*, 1998, **83**, 5609-5620.
63 P. J. A. van Schendel, H. J. Hug, B. Stiefel, S. Martin and H.-J. Güntherodt, *J. Appl. Phys.*, 2000, **88**, 435-445.
64 R.-W. Li, Z.-R. Zhang, Q.-A. Li, J.-R. Sun, G.-J. Wang, Z.-H. Cheng, Z.-H. Wang, S. Y. Zhang, B.-S. Han and B.-G. Shen, *J. Appl. Phys.*, 2002, **92**, 7404-7407.
65 J. Kim, N. Haberkorn, L. Civale, E. Nazaretski, P. Dowden, A. Saxena, J. D. Thompson and R. Movshovich, *Appl. Phys. Lett.*, 2012, **100**, 022407.
66 A. Alberca, C. Munuera, J. Azpeitia, B. Kirby, N. M. Nemes, A. M. Perez-Muñoz, J. Tornos, F. J. Mompean, C. Leon, J. Santamaria and M. Garcia-Hernandez, *Sci. Rep.*, 2015, **5**, 17926.
67 Y. Zhu, K. Du, J. Niu, L. Lin, W. Wei, H. Liu, H. Lin, K. Zhang, T. Yang, Y. Kou, J. Shao, X. Gao, X. Xu, X. Wu, S. Dong, L. Yin and J. Shen, *Nat. Commun.*, 2016, **7**, 11260.
68 N. Rossi, F. R. Braakman, D. Cadeddu, D. Vasyukov, G. Tütüncüoglu, A. Fontcuberta i Morral and M. Poggio, *Nat. Nanotechnol.*, 2017, **12**, 150-155.
69 L. M. de Lépinay, B. Pigeau, B. Besga, P. Vincent, P. Poncharal and O. Arcizet, *Nat. Nanotechnol.*, 2017, **12**, 156-162.
70 J. M. De Teresa, A. Fernández-Pacheco, R. Córdoba, L. Serrano-Ramón, S. Sangiao and M. R. Ibarra, *J. Phys. D: Appl. Phys.*, 2016, **49**, 243003.
71 N. H. Freitag, C. F. Reiche, V. Neu, P. Devi, U. Burkhardt, C. Felser, D. Wolf, A. Lubk, B. Büchner and T. Mühl, *Commun. Phys.*, 2023, **6**, 11.

 This journal is © The Royal Society of Chemistry 20xx

Please do not adjust margins

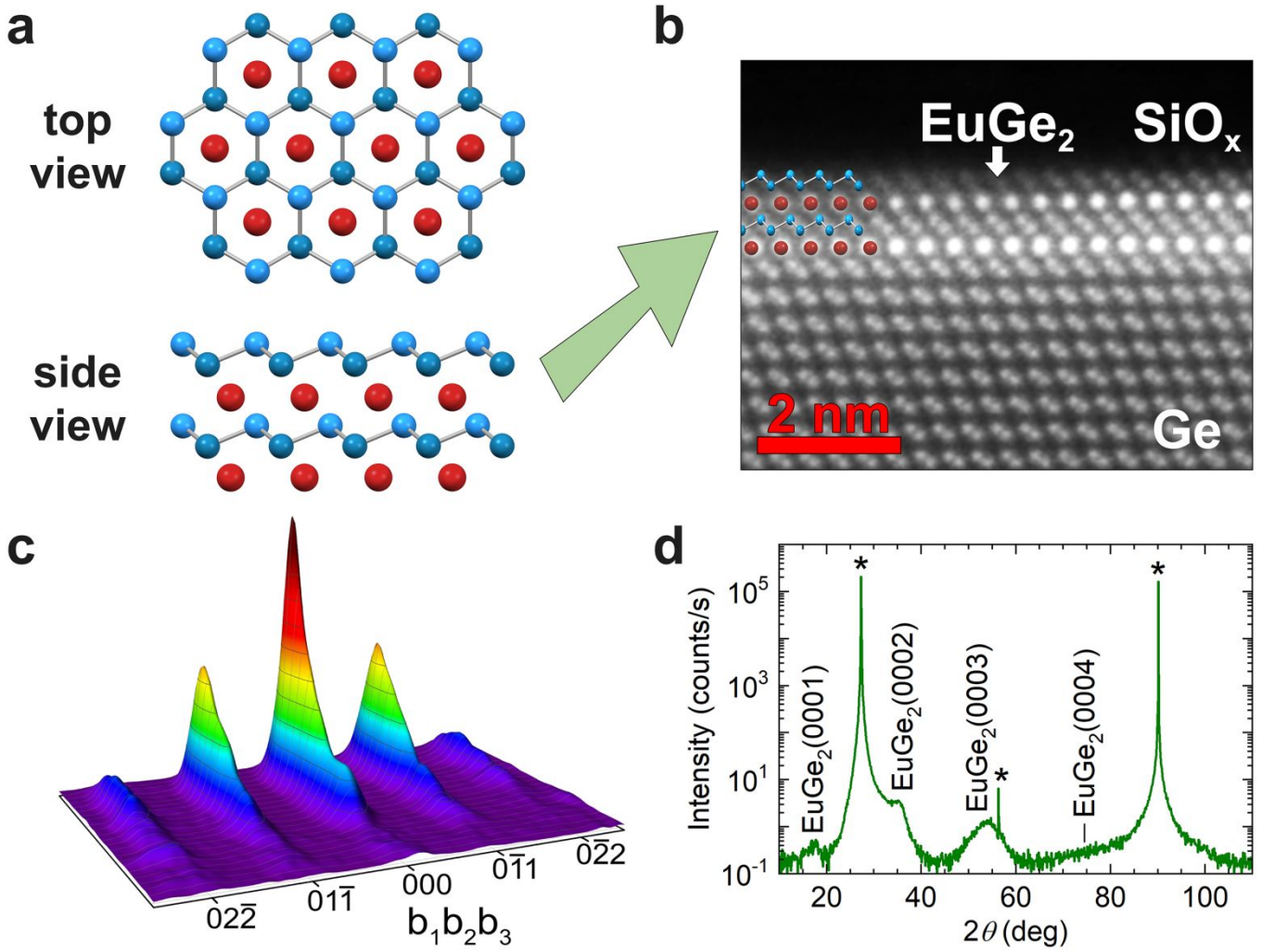

Fig. 1. Atomic structure of 2 ML $EuGe_2$ film on Ge(111). a) Ball-and-stick model (Eu – red and Ge – blue) comprising top view and side view. b) Cross-sectional HAADF-STEM image of the film; the ball-and-stick model is superimposed upon a part of the $EuGe_2$ bilayer image. c) 3D RHEED image of the film; the reflexes are marked by Miller-Bravais indices for the basal plane. d) θ-2θ XRD scan of the film; asterisks denote peaks from the Ge(111) substrate.

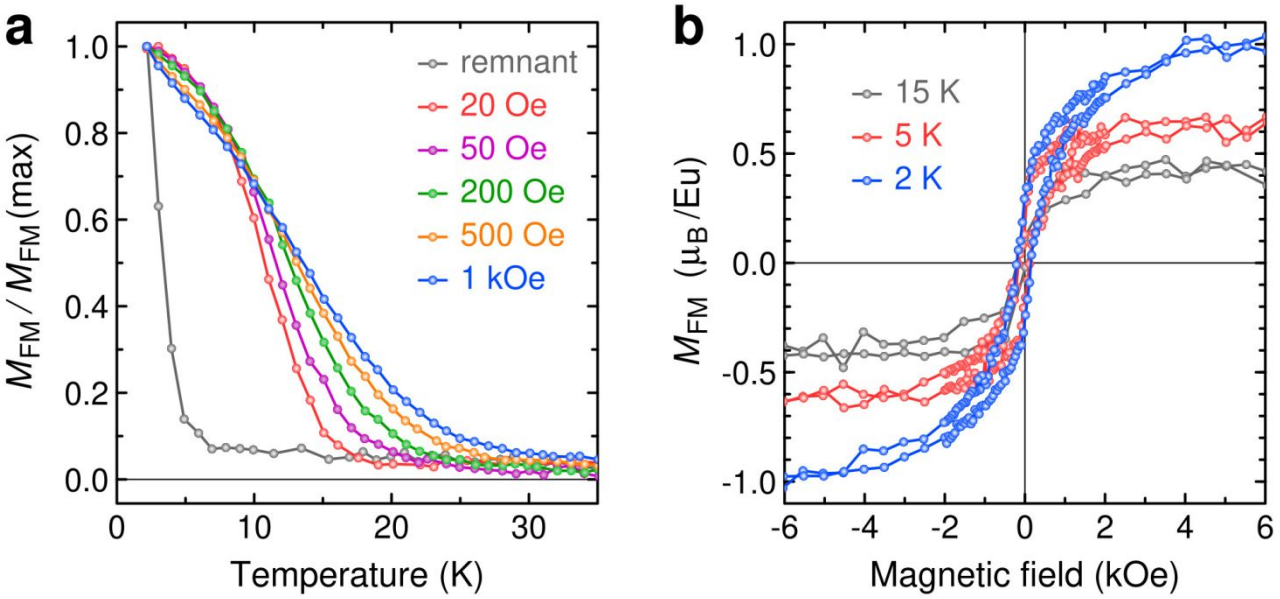

Fig. 2. Magnetic properties of 2 ML $EuGe_2$. a) The normalized FM moment in in-plane magnetic fields 20 Oe (red), 50 Oe (purple), 200 Oe (green), 500 Oe (orange) and 1 kOe (blue) as well as the remnant moment (grey). b) *M-H* hysteresis loops at 2 K (blue), 5 K (red) and 15 K (grey).

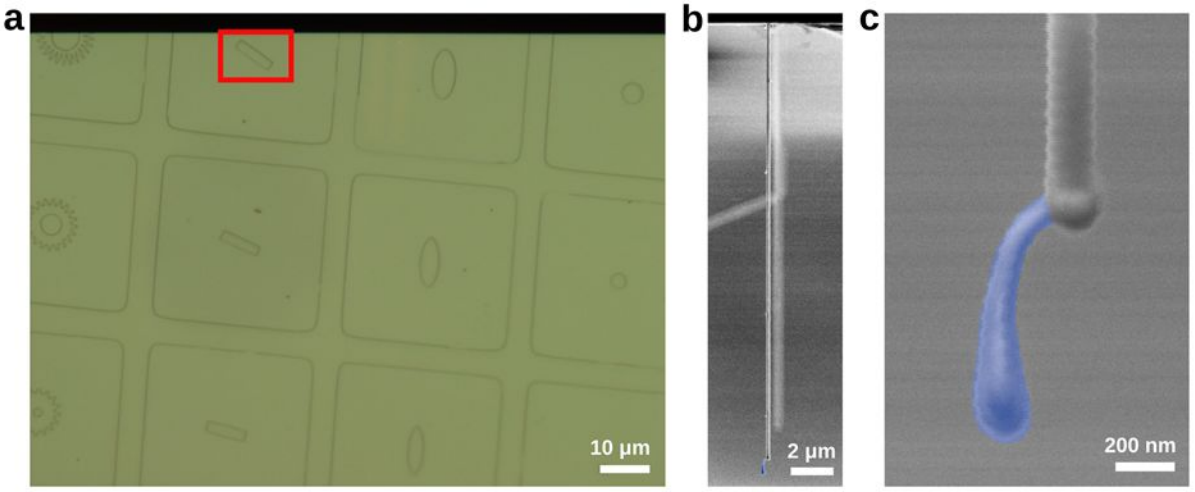

Fig. 3. a) Optical microscope image of the $EuGe_2$ structure array. The measurements presented in this work are performed on the bar indicated by a red frame. b) and c) SEM micrographs of the Si nanowire probe used for the measurements. The magnetic cobalt tip is highlighted in blue.

This journal is © The Royal Society of Chemistry 20xx

Please do not adjust margins

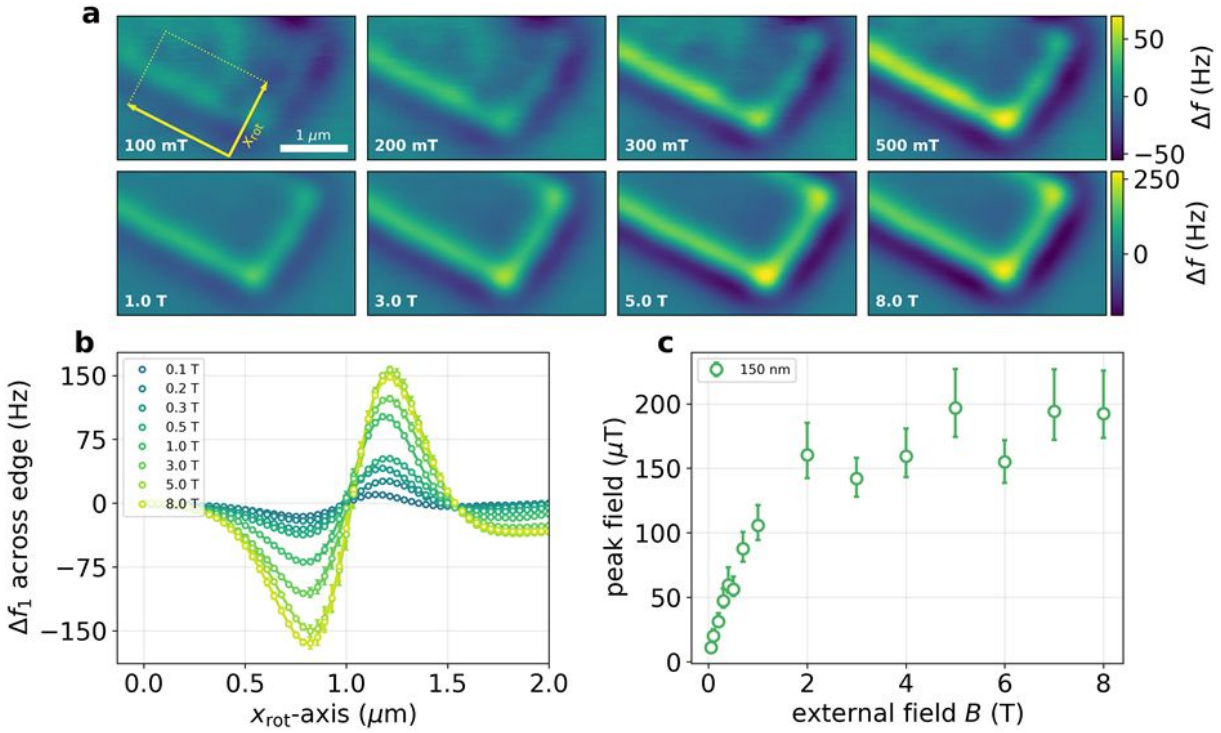

Fig. 4. MFM imaging in different magnetic fields at 4.7 K. a) Frequency shift Δf images at a distance of d = 210 nm for increasing out-of-plane magnetic field B. Note that the scale bar range is larger for the second row of data. b) Line cuts of the first mode frequency shift taken along the x_{rot}-axis, which is almost aligned with the oscillation direction x_1 of the first mode, and averaged over the direction of the sample edge, as indicated in the first image at B = 100 mT. The solid lines connecting the data points act as a guide to the eye. A higher external field leads to a larger frequency shift amplitude across the edge of the bar structure. c) Peak magnitude of the sample magnetic field across the edge at 150 nm tip-sample distances as inferred from the line cuts using a magnetic monopole model for the tip-sample interaction of the NW probe.

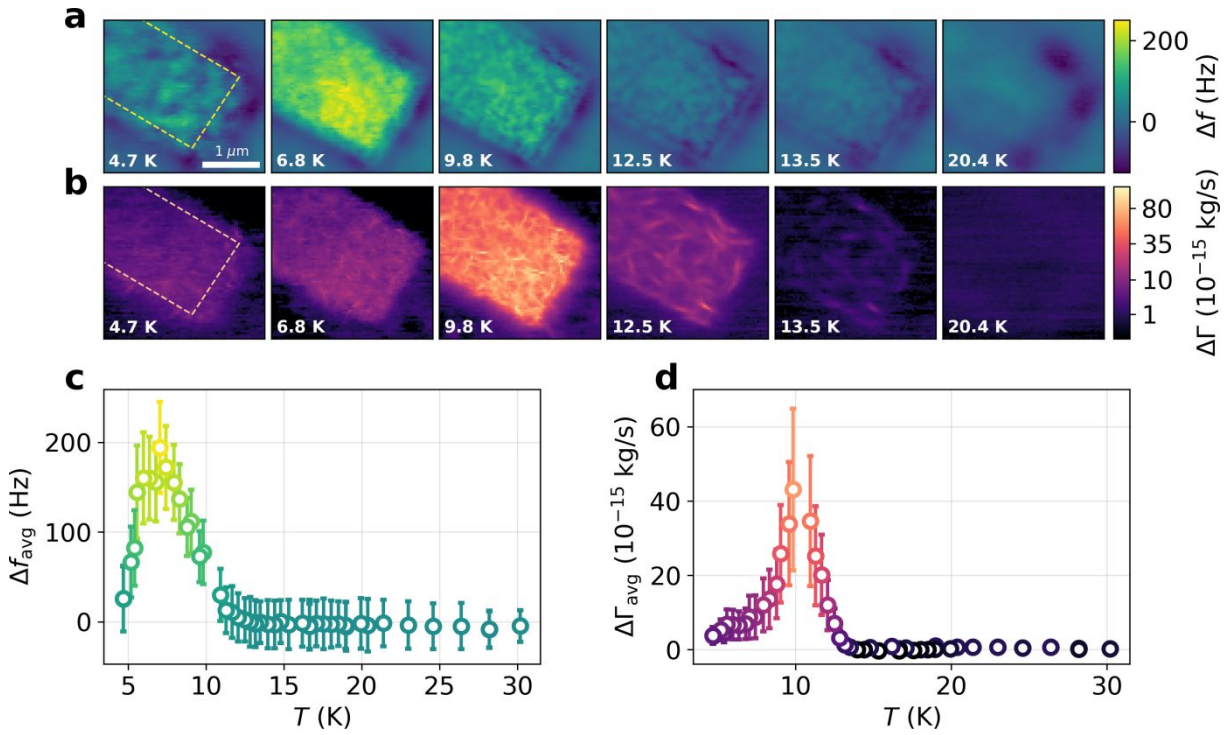

Fig. 5. Temperature-dependent scans of the end section of the bar at zero field and a distance of d = 100 nm. The top row of images a) shows the frequency shift of both modes Δf and the bottom row b) the root mean square dissipation $\Delta\Gamma$ of both modes at different sample temperatures. c) Combined frequency shift averaged over the area of the structure as marked by the yellow box in the first image at 4.7 K. A maximum in the frequency shift appears at $T \approx 6.8$ K. d) Average value of the root mean square dissipation exhibiting a maximum at $T \approx 10$ K.

This journal is © The Royal Society of Chemistry 20xx